ACS OMEGA

http://pubs.acs.org/journal/acsodf

Article

Facile Preparation of Tannic Acid-Gold Nanoparticles for Catalytic and Selective Detection of Mercury(II) and Iron(II) Ions in the Environmental Water Samples and Commercial Iron Supplement

Kun-Yu Sun, Chen-Yu Chueh, Mei-Yao Wu, Tsunghsueh Wu, and Yang-Wei Lin*

Cite This: *ACS Omega* 2024, 9, 41521−41531

Read Online

ABSTRACT: Tannic acid (TA), a plant-derived polyphenol rich in hydroxyl groups, serves as both a reducing agent and stabilizer for synthesizing gold nanoparticles (TA-AuNPs). This study presents a groundbreaking method that utilizes TA to fabricate TA-AuNPs and develop two distinct colorimetric detection systems for mercury (Hg^{2+}) and iron (Fe^{2+}) ions. The first detection system leverages the interaction between TA-AuNPs and Hg^{2+} to enhance the peroxidase-like activity of TA-AuNPs, facilitating the production of hydroxyl radicals upon reaction with hydrogen peroxide, which subsequently oxidizes 3,3′,5,5′-tetramethylbenzidine (TMB) into a blue-colored product (ox-TMB). The second system capitalizes on TA-AuNPs to catalyze the Fenton reaction between Fe^{2+} and hydrogen peroxide in the presence of 2, 6-pyridinedicarboxylic acid, boosting the generation of hydroxyl radicals that oxidize TMB into a blue-colored ox-TMB. Absorbance measurements at 650 nm display a linear relationship with Hg^{2+} concentrations ranging from 0.40 to 0.60 μM ($R^2 = 0.99$) and Fe^{2+} concentrations from 0.25 to 2.0 μM ($R^2 = 0.98$). The established detection limits for Hg^{2+} and Fe^{2+} are 18 nM and 96 nM, respectively. Applications to real-world samples achieved an excellent spiked recovery, spanning 101.6% to 108.0% for Hg^{2+} and 90.0% to 112.5% for Fe^{2+}, demonstrating the method's superior simplicity, speed, and cost-effectiveness for environmental monitoring of these ions compared to existing techniques.

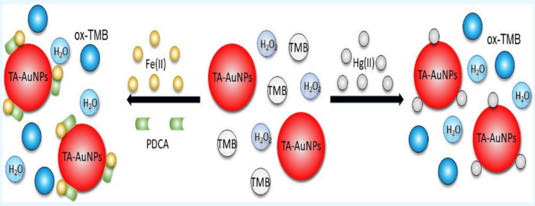

1. INTRODUCTION

Rapid growth in manufacturing brings job opportunities to society. Still, without environmental regulation, it also likely creates environmental pollution, especially polluted water resources with heavy metals such as mercury, lead, cadmium, chromium, and arsenic, substantially threatening aquatic life and human health.[1] Mercury exposure, for example, can lead to severe health issues, including central nervous system defects, cardiac abnormalities, and kidney damage.[2] Intake of Mercury by microorganisms allows the transformation of mercury to lipophilic methylmercury, a potent neurotoxin that enters the human body through the food chain.[3,4] Therefore, detecting mercury in natural water is critical to combating mercury pollution. On the other hand, iron is an essential element for human health and is crucial in energy metabolism, immune response, DNA synthesis, and oxygen transport.[5] However, excessive iron levels in the body have been linked to various neurodegenerative diseases, highlighting the importance of iron detection.[6] Current methods for detecting mercury and iron include ion chromatography, high-performance liquid chromatography, atomic absorption spectroscopy, electrochemistry, and inductively coupled plasma mass spectrometry.[7−10] While effective, these techniques incur limitations such as high cost, complexity, and lengthy detection times, unfit for portable detection. Therefore, there is a pressing need to develop portable detection methods that are cost-effective, highly selective, sensitive, and capable of rapid analysis.

Colorimetric detection, which relies on the visual change in color as a detection criterion, offers a simple, cost-effective, and rapid alternative to existing instrumental methods.[11,12] Techniques for heavy metal ion detection based on UV−visible spectrophotometry or visual inspection are gaining attention due to their simplicity and detector-free readout strategy. The focus on nanomaterial-based colorimetric methods, particularly those utilizing gold nanoparticles (AuNPs), stems from their small size, large surface area, and ease of modification, significantly enhancing the sensitivity and selectivity of colorimetric assays.[13−15] We acknowledge that gold is indeed expensive, and this is a notable disadvantage. However, we utilize a minimal amount of $HAuCl_4 \cdot 3H_2O$ to prepare the AuNPs solution, which can be stored in a dark room for at least three months. Despite the associated cost, the use of AuNPs offers several unique advantages that justify their application in our study. AuNPs exhibit unique properties such

Received: June 2, 2024
Revised: July 3, 2024
Accepted: August 21, 2024
Published: August 27, 2024

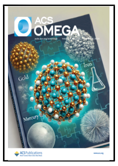

https://doi.org/10.1021/acsomega.4c05167
ACS Omega 2024, 9, 41521−41531

as localized surface plasmon resonance (LSPR) and enzymatic-like activity, making them ideal for developing colorimetric detection systems. Despite the advantages of nanomaterials, challenges remain to be addressed, such as the low catalytic activity of AuNPs compared to natural enzymes, necessitating modifications to improve their performance.[16,17] Previous studies have illustrated the significant potential of AuNPs in colorimetric detection, revealing their interactions with specific ions can markedly enhance their catalytic activity.[18−21] This enhancement is primarily attributed to the unique electronic properties of AuNPs, which facilitate electron transfer processes critical for catalytic reactions.[22,23] However, leveraging the catalytic properties of AuNPs for colorimetric detection is challenging.[24−27] One significant hurdle is the synthesis of AuNPs, which often requires precise control over the nanoparticles' size, shape, and surface chemistry to achieve the desired catalytic activity and stability. The synthesis process can be intricate and time-consuming, with parameters such as temperature, reducing agent concentration, and reaction time playing critical roles in determining the nanoparticles' properties.[28] Additionally, the stability of AuNPs in various environments presents another challenge. Nanoparticles can aggregate in solution, leading to a loss of surface area and, consequently, catalytic activity.[29,30] This aggregation is influenced by factors such as ionic strength, pH, and the presence of specific ions, which can bind to the nanoparticles' surface and induce changes in their physicochemical properties.[31]

To bridge the gap in current detection methodologies, this investigation endeavors to craft an innovative colorimetric detection for mercury (Hg^{2+}) and iron (Fe^{2+}) ions, employing tannic acid-gold nanoparticles (TA-AuNPs). Recognizing the complexities and stability issues inherent in nanoparticle synthesis, the study is dedicated to refining the synthesis and functionalization processes of TA-AuNPs.[32,33] Through meticulous adjustment of synthesis parameters and the implementation of effective stabilization techniques, the goal is to establish a colorimetric detection system that is both highly efficient and reliable. This novel system aspires not only to surmount the prevalent challenges faced by nanoparticle-based sensors but also to broaden the utility of TA-AuNPs for detecting heavy metal ions and beyond.[34,35] By harnessing the distinct attributes of TA-AuNPs, the research aims to deliver swift, precise, and selective detection capabilities suitable for application in analyzing real-world samples. This endeavor is poised to significantly enhance environmental surveillance and deepen our understanding of metal ion detection mechanisms, thereby setting the stage for further innovations in the domain.

2. EXPERIMENT

2.1. Chemicals. The experimental reagents used in this study, including Gold(III) chloride trihydrate ($HAuCl_4 \cdot 3H_2O$), tannic acid (TA), 3,3′,5,5′-tetramethylbenzidine (TMB), hydrogen peroxide (H_2O_2), 2, 6-pyridinedicarboxylic acid (PDCA), hydroquinone (HQ), mercury(II) chloride ($HgCl_2$), barium chloride ($BaCl_2$), anhydrous iron(III) chloride ($FeCl_3$), copper(II) chloride ($CuCl_2$), magnesium chloride hexahydrate ($MgCl_2 \cdot 6H_2O$), tin(II) chloride dihydrate ($SnCl_2 \cdot 2H_2O$), iron(II) chloride tetrahydrate ($FeCl_2 \cdot 4H_2O$), cobalt nitrate hexahydrate ($Co(NO_3)_2 \cdot 6H_2O$), cadmium(II) nitrate tetrahydrate ($Cd(NO_3)_2 \cdot 4H_2O$), nickel(II) nitrate hexahydrate ($Ni(NO_3)_2 \cdot 6H_2O$), lead nitrate ($Pb(NO_3)_2$), sodium chloride (NaCl), calcium chloride dihydrate ($CaCl_2 \cdot 2H_2O$), zinc perchlorate hexahydrate ($Zn(ClO_4)_2 \cdot 6H_2O$), silver nitrate ($AgNO_3$), and potassium nitrate (KNO_3), were all acquired from Sigma-Aldrich (St. Louis, MO, USA). These chemicals, utilized throughout our experiments, were of analytical grade or the highest available purity. Milli-Q deionized water was used exclusively for all experimental procedures.

2.2. Characterization. The characterization of the prepared AuNPs was meticulously carried out using various advanced analytical techniques. Optical properties were evaluated by recording UV−visible spectra on an Evolution 200 UV−vis spectrophotometer (ThermoFisher Scientific, NY, USA). The crystallographic structures of the prepared AuNPs were determined via X-ray diffraction (XRD) utilizing a LabX XRD-6000 X-ray diffractometer (Shimadzu Corporation, Kyoto, Japan). Identification of organic functional groups decorating the prepared AuNPs was achieved through Fourier Transform Infrared (FT-IR) spectroscopy, conducted on an Agilent Cary 600 series FT-IR spectrometer (Agilent Technologies, California, USA). The morphology and microstructure of the prepared AuNPs were closely examined using Transmission Electron Microscopy (TEM) on a JEOL-1200EX II system (JEOL Ltd., Tokyo, Japan), while a Hitachi S-4300 scanning electron microscope (SEM) (Hitachi High Technologies Corporation, Tokyo, Japan), equipped with a QUANTAX Annular XFlash QUAD FQ5060 energy-dispersive X-ray spectroscopy (EDX) detector (Bruker Nano GmbH, Berlin, Germany) and operating at an acceleration voltage of 15 kV, provided detailed insights into the morphology and elemental composition of the prepared AuNPs.

2.3. Synthesis of TA-AuNPs. Tannic acid-modified gold nanoparticles (TA-AuNPs) were synthesized by heating 48 mL of $HAuCl_4 \cdot 3H_2O$ solution (0.13 mM) to boiling. Subsequently, 2 mL of TA solution (6.0 mM) was added to the boiling solution. The mixture was then stirred and heated for another 2 min to facilitate the reaction. Upon completion of the reaction, a red-wine-colored solution was achieved, which was then allowed to cool to room temperature. This study defined the prepared quantity of TA-AuNPs as 1 ×.

2.4. Kinetic Study. To elucidate the reaction mechanism of ion detection in this study, the interaction between peroxidase-mimicking agents and the substrates TMB and H_2O_2 was explored using the Michaelis−Menten equation. This equation is represented as $V_0 = \frac{V_{max} + [S]}{K_m + [S]}$, where V_0 is the initial reaction rate, V_{max} is the maximum rate achieved by the system at maximum (saturating) substrate concentration, K_m is the Michaelis constant indicative of the enzyme's affinity for the substrate, and [S] is the substrate concentration. Assuming TA-AuNPs/Hg and TA-AuNPs/PDCA/Fe systems function as peroxidase enzymes with TMB and H_2O_2 acting as the substrates, the substrate concentration varied while keeping the enzyme concentration constant. The reaction was monitored over 5 min by taking absorbance readings every minute. These absorbance values were used to calculate the concentration of oxidized TMB (ox-TMB) according to Beer's law ($A = \varepsilon bC$), where A is absorbance, ε is the molar extinction coefficient, b is the path length of light through the sample, and C is the concentration of the absorbing species in the sample. A plot of ox-TMB concentration against time yielded slopes equivalent to V_0 for generating a series of V_0 values. The Lineweaver−Burk plot, a double reciprocal graph of $1/V_0$ against $1/[S]$,

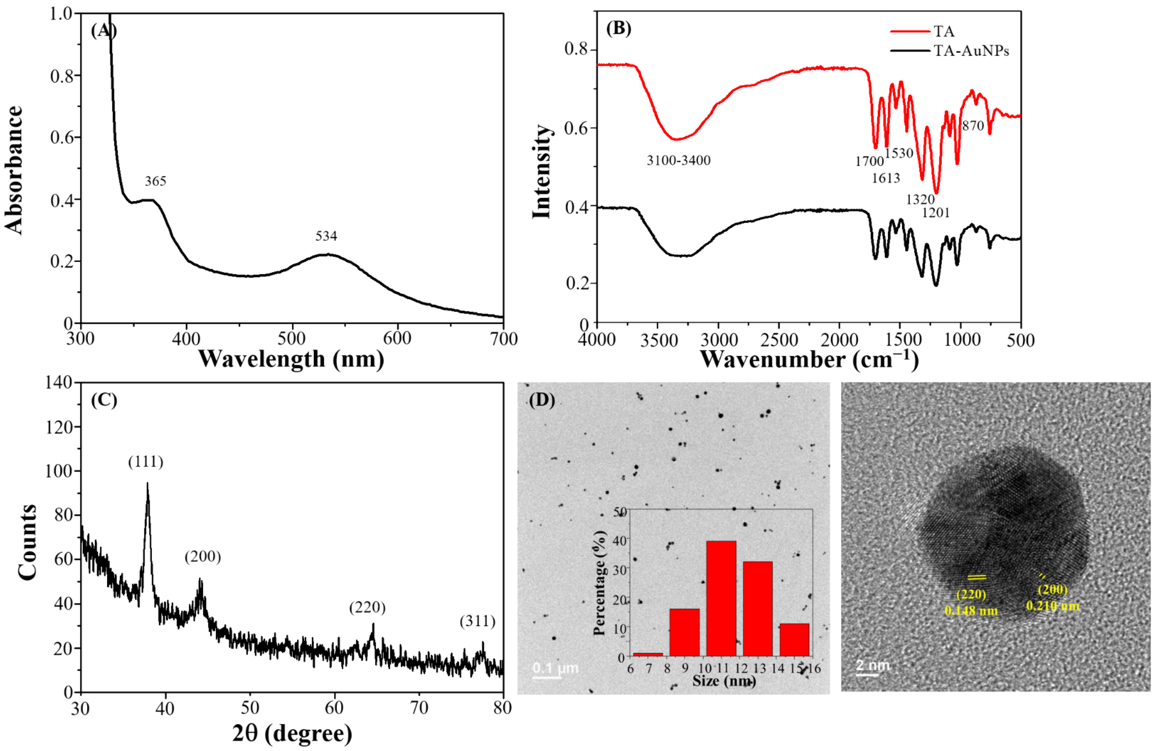

Figure 1. Characterization of TA-AuNPs. (A) UV−vis spectrum, (B) FT-IR spectra (TA: red), (C) XRD patterns, and (D) TEM images (inset: particle size distribution).

facilitated the determination of $1/V_{max}$ and $1/K_m$ from the y-intercept and x-intercept, respectively.

2.5. Sensing Process. The mercury sensing process was conducted by preparing solutions of Hg^{2+} ranging from 4.0 to 6.0 μM in deionized water, 0.5 M H_2O_2, and 10 mM TMB in acetone. The procedure involved adding 600 μL of deionized water, 100 μL of the Hg^{2+} solution, 100 μL of 1× TA-AuNPs, 100 μL of TMB, and 100 μL of H_2O_2 sequentially to form a mixture. After vigorous shaking, the reaction proceeded for 10 min at room temperature. Upon completion, 200 μL of the solution was transferred to a 96-well plate to measure the absorbance peak at 650 nm.

The iron sensing procedure was executed by preparing solutions of Fe^{2+} in the concentration range of 2.5−20 μM in deionized water, accompanied by 0.5 M H_2O_2 and 10 mM PDCA in acetone, along with 10 mM TMB. The process entailed sequentially mixing 500 μL of deionized water, 100 μL of the Fe^{2+} solution, 100 μL of PDCA, 100 μL of 1× TA-AuNPs, 100 μL of TMB, and 100 μL of H_2O_2 to form a mixture. Following agitation, the mixture was allowed to react for 10 min. At the end of the reaction, 200 μL of the solution was pipetted into a 96-well plate to measure the absorbance peak at 650 nm.

2.6. Real Sample Pretreatment. For the spiked recovery test, the pretreatment of actual lake water samples involved collecting water from Baisha Lake at the National Changhua University of Education. The collected lake water was centrifuged at 5,000 rpm for 15 min to separate the supernatant from particulates. Subsequently, the supernatant was filtered through a 0.2 μm pore size filter membrane to ensure clarity. The filtered lake water was then diluted 10-fold and used to prepare solutions containing Hg^{2+} and Fe^{2+} metal ions. These prepared solutions underwent metal ion detection using the previously described methods for TA-AuNPs, allowing for assessing Hg^{2+} and Fe^{2+} concentrations.

In the case of commercial iron supplements, the preparation involved grinding the tablets to a fine powder, dissolving them in deionized water, and filtering through a 0.2 μm membrane to eliminate insoluble material. The resultant solution was diluted 100-fold and spiked with additional Fe^{2+} to perform a standard addition analysis employing the TA-AuNPs method for Fe^{2+} detection.

3. RESULTS AND DISCUSSION

3.1. Characterization. Figure 1A presents the absorption spectrum of TA-AuNPs, showcasing the characteristics of surface plasmon resonance (SPR), such as intensity and bandwidth. These SPR features can be modulated by factors including the size and shape of the nanoparticles, the dielectric constant of the medium, and the temperature.[36] The SPR band also aids in assessing the dispersity of the nanoparticles, where a sharp absorption band at 534 nm suggests the predominance of spherical nanoparticles. The additional absorption peak at 365 nm is ascribed to hydroxyl groups linked with galloyl residues from TA, indicating the successful attachment of TA on AuNPs.[37]

Fourier-transform infrared spectroscopy (FTIR) was applied to confirm TA's role in reducing and stabilizing AuNPs by identifying specific functional groups on the TA-AuNPs surface. Peaks in Figure 1B reveal various functional groups are present: the 1700 cm^{-1} peak corresponds to the carboxylic C=O stretch, the 1613 cm^{-1} peak to C=C stretches in aromatic rings, and peaks at 1320 and 870 cm^{-1} to C−O stretches and O−H out-of-plane bends in TA, respectively.[38] A peak at 1201 cm^{-1} indicates C−O stretching vibrations in polyols. Overlaps between TA and TA-AuNP peaks confirm TA's efficacy in reducing and stabilizing AuNPs.

The X-ray powder diffraction (XRD) analysis, as depicted in Figure 1C, authenticated the successful synthesis and crystalline nature of TA-AuNPs by aligning distinct signals at 37.88°, 44.00°, 64.56°, and 78.68° with the (111), (200), (220), and (311) planes, respectively, (JCPDS: 04−0784), affirming the face-centered cubic (FCC) structure of TA-AuNPs.[32] TEM analysis, illustrated in Figure 1D, indicated spherical TA-AuNPs with an average diameter of approximately 11.6 ± 3.2 nm. Lattice fringes at 0.210 and 0.148 nm correlate with the (200) and (220) crystal planes, respectively, corroborating the XRD findings and supporting the successful synthesis and crystalline nature of the TA-AuNPs.

To ascertain the superior stability of TA-AuNPs, a comparative analysis against traditional sodium citrate-synthesized AuNPs (SC-AuNPs) under various pH and salinity scenarios was conducted. Figures S1A and 1B display that both TA-AuNPs and SC-AuNPs maintain commendable stability within the pH range of 5.0 to 9.0. However, Figures S1C and 1D illustrate that TA-AuNPs exhibit enhanced stability in environments containing 40.0 mM NaCl, surpassing the SC-AuNPs. This superior salinity resistance of TA-AuNPs, as opposed to SC-AuNPs, underscores the beneficial impact of utilizing TA in AuNPs synthesis. The improved salt tolerance can be attributed to the molecular structure of TA, which can form a dense and voluminous coating around the AuNPs and offer steric hindrance that mitigates nanoparticle aggregation under high-salinity conditions.[39] Furthermore, the multiple phenolic groups in TA molecules establish a stronger bond to the gold surface compared to the simpler citrate ions, resulting in a sturdier and more protective layer that enhances nanoparticle dispersion in saline solutions.

3.2. Sensing Approach. In this study, we delineated two specific mechanisms for detecting Hg^{2+} and Fe^{2+} ions via TA-AuNPs, as depicted in Schematic 1. The mechanism targeting Hg^{2+} entails the interaction between TA-AuNPs and Hg^{2+}, forming an Au−Hg amalgam.[40] This interaction notably enhances the peroxidase-mimetic activity of the nanoparticles, which, in the presence of H_2O_2, catalyzes the generation of hydroxyl radicals. These radicals subsequently oxidize TMB, resulting in a detectable color shift from colorless to blue within the solution. Conversely, the detection strategy for Fe^{2+} involves PDCA-mediated chelation of Fe^{2+} ions, amplifying the Fenton reaction and thus producing an increased quantity of hydroxyl radicals.[41] These radicals aid in the oxidation of TMB, resulting in the appearance of a blue color. In addition, TA reduces Fe^{3+} to Fe^{2+}, fostering a continuous Fenton reaction cycle.[42] This feedback loop significantly bolsters the colorimetric signal, enabling efficient detection of Fe^{2+} ions.

To substantiate our hypothesis, UV−vis spectroscopy was utilized to monitor the SPR peak alterations of TA-AuNPs with the incorporation of metal ions, as depicted in Figure 2. Initially, TA-AuNPs showcased a definitive SPR peak at 534 nm in the absence of metal ions (black spectrum in Figure 2). The introduction of Hg^{2+} led to a notable peak shift to 524 nm (red spectrum in Figure 2), signifying a pronounced interaction and subsequent amalgamation formation between Au and Hg^{2+}, modifying the TA-AuNPs' surface and causing the peak displacement. Such a shift was not evident in the scenarios involving TA-AuNPs + Fe^{2+} (blue spectrum in Figure 2), TA-AuNPs + PDCA + Hg^{2+} (green spectrum in Figure 2), and TA-AuNPs + PDCA + Fe^{2+} (pink spectrum in Figure 2), reinforcing that the unique affinity between Au and Hg^{2+} instigates the observed spectral changes. Introducing PDCA, which sequesters Hg^{2+} from interacting with TA-AuNPs, mitigated the amalgamation process, negating significant peak displacement.[43−45] The nonoccurrence of a similar shift with the TA-AuNPs/PDCA/Fe system further delineates the distinct detection mechanisms for Hg^{2+} and Fe^{2+}, highlighting the exclusive interaction specificity between TA-AuNPs and Hg^{2+}.

Scheme 1. Detection Scheme Utilizes TA-AuNPs/H_2O_2/TMB and TA-AuNPs/PDCA/H_2O_2/TMB for Hg^{2+} and Fe^{2+} Ions, Respectively

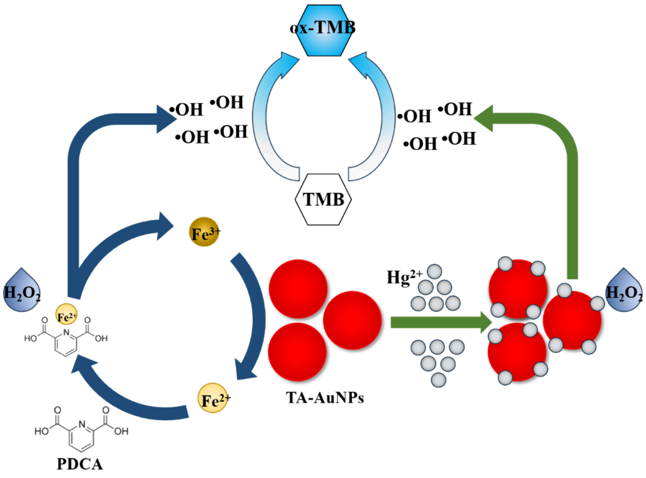

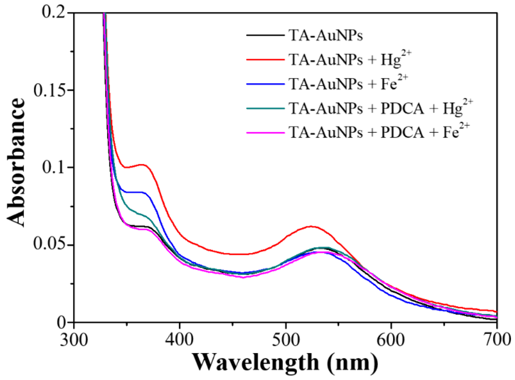

Figure 2. UV−vis spectra under various conditions: TA-AuNPs (black), TA-AuNPs + Hg^{2+} (red), TA-AuNPs + Fe^{2+} (blue), TA-AuNPs + PDCA + Hg^{2+} (green), and TA-AuNPs + PDCA + Fe^{2+} (pink).

In this investigation, we scrutinized the Hg^{2+} detection using the TA-AuNPs/H_2O_2/TMB system. Figure 3A illustrates the absorbance changes within this system in the presence and absence of Hg^{2+} ions. The data reveal that Hg^{2+} ions facilitate the formation of TA-AuNPs/Hg amalgam, showcasing peroxidase-like functionality by catalyzing the oxidation of TMB, which results in the generation of a blue-colored oxidized TMB (ox-TMB) product. A pronounced absorption peak marks this chemical transformation at 650 nm. Since the reaction could be retarded by HQ, a free radical scavenger,[46] it was supposed that the processes might occur via a free radical reaction route, as shown in Figure S2. Figure 3B delves into various mixtures, including a: Hg^{2+} + TMB, b: H_2O_2 + TMB, c: TA-AuNPs + TMB, d: Hg^{2+} + H_2O_2 + TMB, e: Hg^{2+} + TA-AuNPs + TMB, f: TA-AuNPs + H_2O_2 + TMB, and g: Hg^{2+} + TA + H_2O_2 + TMB. None of these manifested a catalytic effect to produce an absorption peak at 650 nm. The TEM and SEM

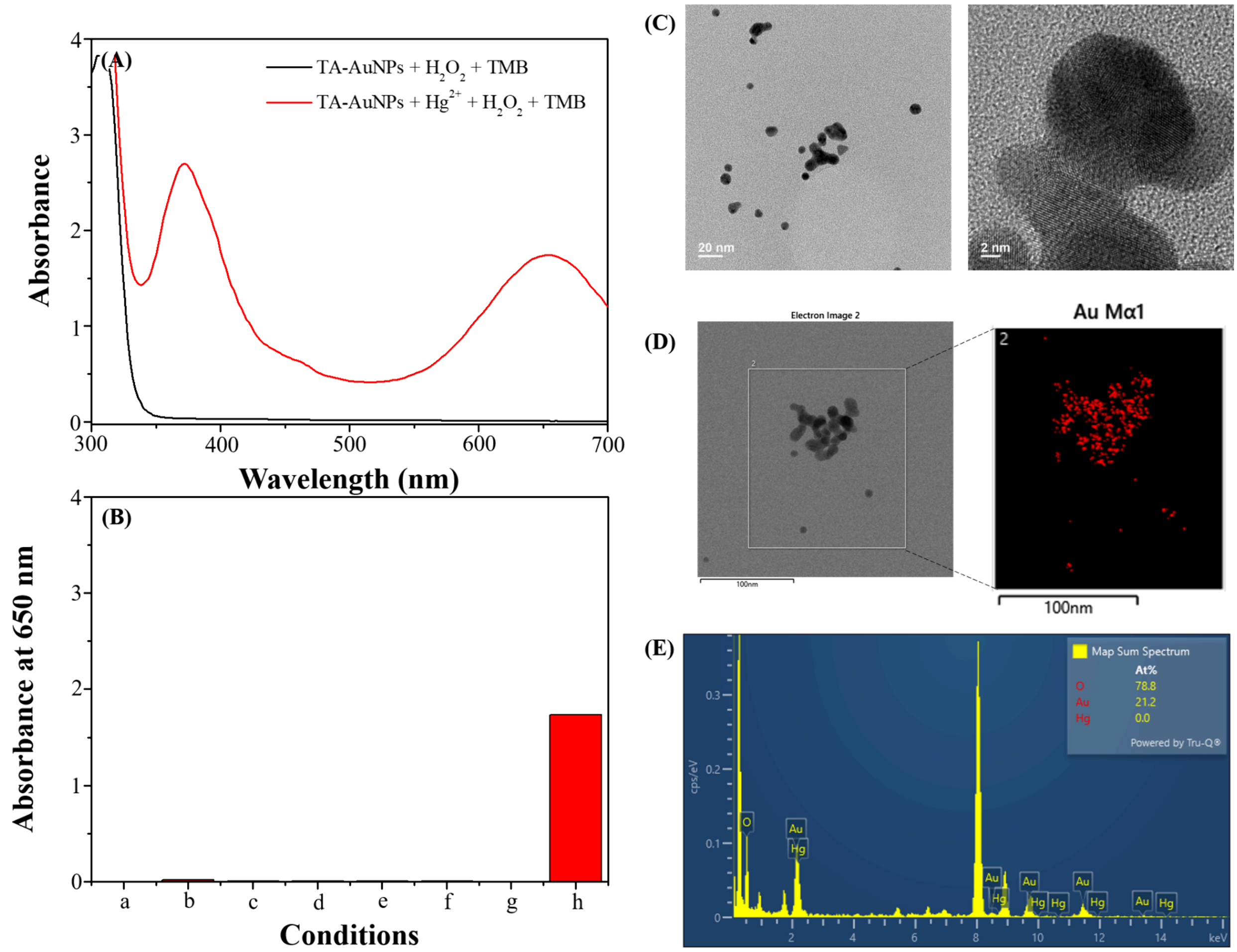

Figure 3. Mercury ion detection. (A) UV−vis spectra of TA-AuNPs/H_2O_2/TMB in the absence (black) and presence (red) of 1.0 μM Hg^{2+} ions; (B) Absorbance at 650 nm under varied conditions a: Hg^{2+} + TMB, b: H_2O_2 + TMB, c: TA-AuNPs + TMB, d: Hg^{2+} + H_2O_2 + TMB, e: Hg^{2+} + TA-AuNPs + TMB, f: TA-AuNPs + H_2O_2 + TMB, g: Hg^{2+} + TA + H_2O_2 + TMB, and h: Hg^{2+} + TA-AuNPs + H_2O_2 + TMB (0.1× TA-AuNPs, [Hg^{2+}]: 1.0 μM, [H_2O_2]: 50 mM, [TMB]: 1.0 mM), (C) TEM, (D) SEM images with elemental mapping, and (E) EDS spectra of TA-AuNPs with 1.0 μM Hg^{2+} ions.

images presented in Figures 3C and 3D, respectively, delineate discernible differences in the size and shape between the TA-AuNPs/Hg nanocomposites and TA-AuNPs (Figure 1D). Surprisingly, the elemental mapping and EDS analyses, as shown in Figures 3D and 3E, failed to register mercury signals. The undetectability of mercury element is speculated to arise from the lower concentration of Hg^{2+} ions introduced, leading to a lower content of Au−Hg amalgam formation on the TA-AuNPs surface, thereby rendering the mercury content undetectable.

Our investigation delved into detecting Fe^{2+} ions utilizing the TA-AuNPs/PDCA/H_2O_2/TMB system. Figure 4A demonstrates the absorbance variations of the system under different conditions. The findings reveal that the simultaneous presence of Fe^{2+} ions and PDCA creates a PDCA-Fe^{2+} complex, catalyzing the Fenton reaction with H_2O_2. This catalysis oxidizes TMB, resulting in a blue-colored ox-TMB product, manifested by a notable absorption peak at 650 nm (red spectrum in Figure 4A). Introducing TA boosts the absorbance at 650 nm by 1.29 times (blue spectrum in Figure 4A), indicating that TA facilitates the electron donation process to reduce Fe^{3+} to Fe^{2+}, thus amplifying the absorbance. Within the TA-AuNPs/PDCA system, the abundant TA molecules on TA-AuNPs surfaces not only serve as a protective layer but also engage in the reduction reaction, significantly heightening the absorbance at 650 nm approximately 6.99 times compared to that without Fe^{2+} ions (black and green spectrum in Figure 4A). But, this reaction was retarded in the presence of HQ, as shown in Figure S2. Figure 4B investigates various component combinations, revealing that only the specific mixtures (n: Fe^{2+} + PDCA + H_2O_2 + TMB, o: Fe^{2+} + PDCA + TA + H_2O_2 + TMB, p: Fe^{2+} + PDCA + TA-AuNPs + H_2O_2 + TMB) demonstrated a catalytic effect, leading to an absorption peak at 650 nm, while others did not (a: Fe^{2+} + TMB, b: PDCA + TMB, c: TA-AuNPs + TMB, d: H_2O_2 + TMB, e: Fe^{2+} + H_2O_2 + TMB, f: Fe^{2+} + PDCA + TMB, g: Fe^{2+} + TA-AuNPs + TMB, h: PDCA + H_2O_2 + TMB, i: TA-AuNPs + H_2O_2 + TMB, j: PDCA + TA-AuNPs + TMB, k: PDCA + TA-AuNPs + H_2O_2 + TMB, l: Fe^{2+} + TA-AuNPs + H_2O_2 + TMB, m: Fe^{2+} + PDCA + TA-AuNPs + TMB, and n: Fe^{2+} + PDCA + H_2O_2 + TMB). TEM and SEM analyses, presented in Figures 4C and 4D, showing distinguishable differences in size and morphology between TA-AuNPs/Fe/PDCA and TA-AuNPs. Additionally, elemental mapping and EDS (Figures 4D and 4E) assessments confirmed the detection of gold and iron elements, validating the presence of these constituents within the nanostructure.

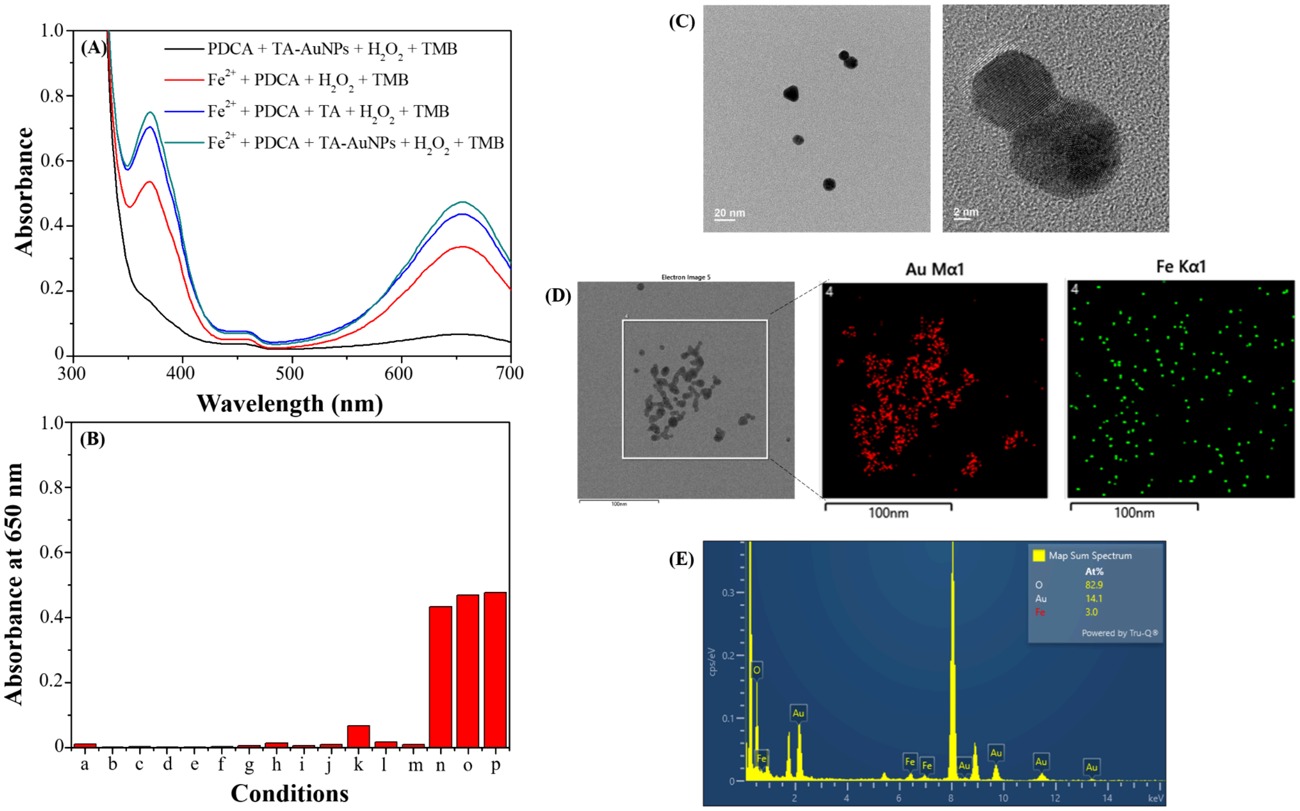

Figure 4. Iron ion detection. (A) UV−vis spectra under various conditions: PDCA + TA-AuNPs + H_2O_2 + TMB (black), Fe^{2+} + PDCA + H_2O_2 + TMB (red), Fe^{2+} + PDCA + TA + H_2O_2 + TMB (blue), and Fe^{2+} + PDCA + TA-AuNPs + H_2O_2 + TMB (green). (B) Absorbance at 650 nm under various conditions: a: Fe^{2+} + TMB, b: PDCA + TMB, c: TA-AuNPs + TMB, d: H_2O_2 + TMB, e: Fe^{2+} + H_2O_2 + TMB, f: Fe^{2+} + PDCA + TMB, g: Fe^{2+} + TA-AuNPs + TMB, h: PDCA + H_2O_2 + TMB, i: TA-AuNPs + H_2O_2 + TMB, j: PDCA + TA-AuNPs + TMB, k: PDCA + TA-AuNPs + H_2O_2 + TMB, l: Fe^{2+} + TA-AuNPs + H_2O_2 + TMB, m: Fe^{2+} + PDCA + TA-AuNPs + TMB, n: Fe^{2+} + PDCA + H_2O_2 + TMB, o: Fe^{2+} + PDCA + TA + H_2O_2 + TMB, p: Fe^{2+} + PDCA + TA-AuNPs + H_2O_2 + TMB (0.1× TA-AuNPs, [PDCA]: 1.0 mM, [Fe^{2+}]: 1.0 μM, [H_2O_2]: 50 mM, [TMB]: 1.0 mM), (C) TEM, (D) SEM images with elemental mapping, and (E) EDS spectrum of TA-AuNPs/PDCA with 1.0 μM Fe^{2+} ions.

3.3. Kinetic Study. To elucidate the reaction mechanisms involved in Hg^{2+} and Fe^{2+} ions detection within this study, we applied the Michaelis−Menten equation to evaluate the interaction between the peroxidase-like activity of TA-AuNPs/Hg and TA-AuNPs/PDCA/Fe with TMB and H_2O_2 as substrates. We measured absorbance every minute over a 5 min reaction by maintaining a constant enzyme concentration while varying substrate concentrations. These absorbance values were converted into concentrations of ox-TMB using Beer's law. From the graph time against ox-TMB concentration, we derived the initial reaction rates (V_0) for various conditions. Subsequently, employing the Lineweaver−Burk double reciprocal plotting method, we graphed $1/V_0$ against $1/[S]$, resulting in the data presented in Figure 5.

From the outcomes depicted in Figure 5, we calculated each system's Michaelis constant (K_m) and maximum velocity (V_{max}), as shown in Table 1. In the TA-AuNPs/Hg system (0.1 × TA-AuNPs + 1.0 μM Hg^{2+}) using TMB as the substrate, we found V_{max} to be 2.34×10^{-7} M·S^{-1} and K_m to be 1.98×10^{-4} M. When H_2O_2 served as the substrate, V_{max} reached 8.06×10^{-7} M·S^{-1} with a K_m value of 1.65×10^{-1} M. The smaller K_m value for TMB indicates a stronger affinity between TA-AuNPs/Hg and TMB, suggesting a favorable interaction with TMB. Similarly, in the TA-AuNPs/PDCA/Fe system (1.0 μM Fe^{2+} + 1.0 mM PDCA + 0.1 × TA-AuNPs), the V_{max} for TMB as the substrate was 3.86×10^{-8} M·S^{-1} with a K_m value of 2.16×10^{-4} M. At the same time, for H_2O_2, V_{max} was 5.95×10^{-7} M·S^{-1} with a K_m value of 6.02×10^{-2} M. Again, the small K_m value for TMB indicates that the TA-AuNPs/PDCA/Fe system has a stronger affinity for TMB, suggesting a preferential interaction with TMB.

Specifically, the TA-AuNPs/Hg system demonstrated a stronger affinity (lower K_m value) for TMB compared to H_2O_2, suggesting that these TA-AuNPs preferentially interact with TMB in the presence of Hg^{2+} ions. This preference underlines the specificity of the TA-AuNPs/Hg system toward TMB, enhancing its efficiency as a sensor for Hg^{2+}. Conversely, the TA-AuNPs/PDCA/Fe system also showed a stronger affinity for TMB over H_2O_2, although with different kinetic values compared to the Hg^{2+} detection system. This differential affinity underscores the distinct mechanisms through which these nanoparticles detect Fe^{2+} ions, likely due to the formation of the PDCA-Fe^{2+} complex, which enhances the Fenton reaction and catalyzes the oxidation of TMB. Applying enzymatic kinetics to these nanomaterial-based detection systems provides valuable insights into their operational mechanisms. It establishes a foundation for further refinement and application of nanoparticle-based sensors in detecting specific metal ions. Furthermore, if the enzyme activity changes, it may alter the structure of the active site or its binding mode to the substrate, thereby affecting the K_m value. Increasing enzyme activity can enhance the reaction rate, increasing V_{max}, whereas decreasing enzyme activity can reduce V_{max}. In our system, the changes in K_m and V_{max} with varying

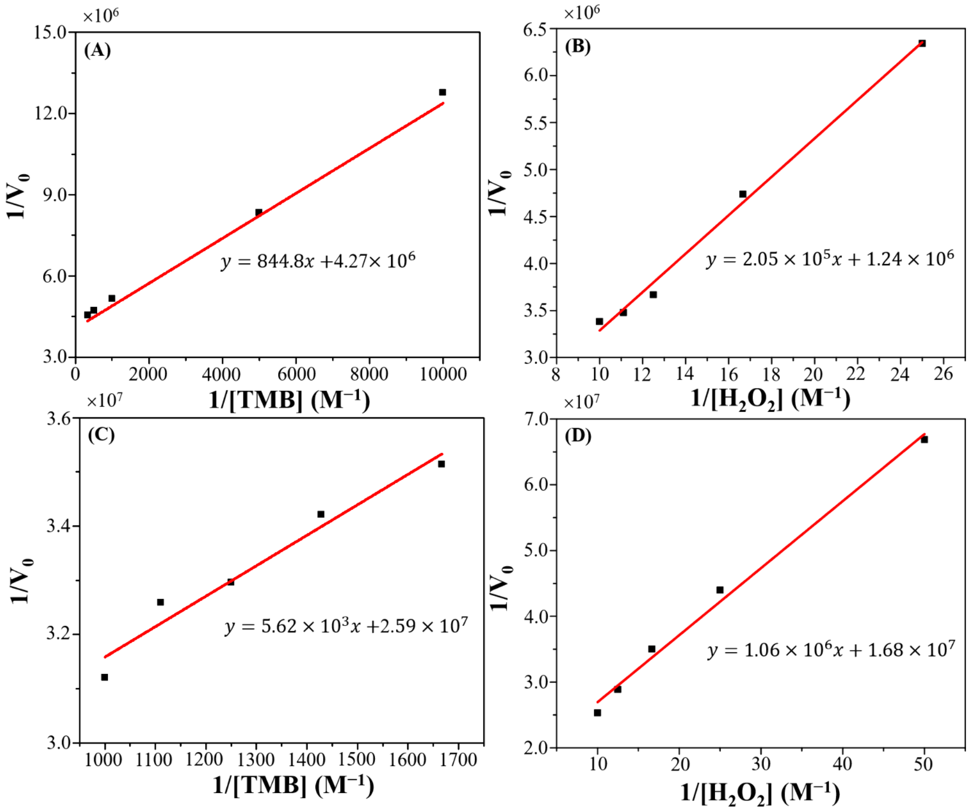

Figure 5. Kinetic analysis. Lineweaver–Burk plots for (A, B) TA-AuNPs/Hg^{2+}/H_2O_2/TMB, and (C, D) TA-AuNPs/PDCA/Fe^{2+}/H_2O_2/TMB systems.

Table 1. Kinetic Parameters of TA-AuNPs in the Absence and Presence of PDCA for Detecting Hg^{2+} and Fe^{2+} Ions

	TMB		H_2O_2	
System	K_m (M)	V_{max} ($M{\cdot}S^{-1}$)	K_m (M)	V_{max} ($M{\cdot}S^{-1}$)
TA-AuNPs/Hg^{2+}	1.98×10^{-4}	2.34×10^{-7}	1.65×10^{-1}	8.06×10^{-7}
TA-AuNPs/PDCA/Fe^{2+}	2.16×10^{-4}	3.86×10^{-4}	6.02×10^{-2}	5.95×10^{-8}

enzyme activities will be a focus of our laboratory's future research.

3.4. Selectivity and Sensitivity. In preparation for real-sample analysis using TA-AuNPs, we evaluated the selectivity of our detection systems against a spectrum of metal ions (Ba^{2+}, Fe^{3+}, Cu^{2+}, Mg^{2+}, Sn^{2+}, Co^{2+}, Ni^{2+}, Pb^{2+}, Na^+, Ca^{2+}, Zn^{2+}, Ag^+, and K^+, all metal ions at 1.0 μM). Figure 6A reveals that the TA-AuNPs/H_2O_2/TMB system is highly selective for Hg^{2+}, attributed to the amalgamation of Hg^{2+} with TA-AuNPs that notably enhances their peroxidase-mimicking activity. Conversely, other tested metal ions did not exhibit this enhancement, failing to generate sufficient hydroxyl radicals for TMB oxidation. As depicted in Figure 6B, the addition of PDCA to the TA-AuNPs/H_2O_2/TMB did not alter the color in the presence of Hg^{2+} solutions, indicating that PDCA's chelation with Hg^{2+} inhibits its amalgamation with TA-AuNPs, thereby preventing the oxidation of TMB. Contrarily, solutions containing Fe^{2+} and Fe^{3+} exhibited a color change to blue, signifying that PDCA's interaction with Fe^{2+} bolsters the Fenton reaction, leading to the generation of hydroxyl radicals and subsequent TMB oxidation. TA molecules contribute to this process by reducing Fe^{3+} to Fe^{2+}, facilitating the reaction and inducing a slight blue color in Fe^{3+} solutions. Due to the stronger absorbance signal from Fe^{2+}, future assays will primarily target Fe^{2+}, although efforts to improve selectivity are recommended for future enhancements. Our laboratory is currently addressing these challenges.

After confirming the selectivity of TA-AuNPs for ion detection, we performed sensitivity tests for both systems to establish the detection of limit (LOD) for Hg^{2+} and Fe^{2+} ions. According to Figure 6C, the absorbance at 650 nm increases with increasing concentrations of Hg^{2+}. The inset in Figure 6C shows a linear response range for Hg^{2+} between 0.40–0.60 μM (R^2 = 0.995), with a LOD of 18 nM (3.61 ppb). This sensitivity aligns with the discharge standards set by Taiwan's Environmental Protection Administration, which stipulates mercury concentrations in industrial effluent must not exceed 5.00 ppb, and the World Health Organization (WHO), along with Taiwan's drinking water standards, mandate mercury levels not to exceed 1.00 ppb.[15] Therefore, this system could be applied for industrial wastewater testing, though further improvements are needed for drinking water analysis. Our laboratory is currently addressing these challenges. In addition, optimization of this linear range is indeed possible and will be another important aspect of our future work. We will aim to prepare TA-AuNPs of an appropriate size and optimize the concentration of the TA-AuNP solution. We believe that modifying the surface-to-volume ratio of TA-AuNPs will extend the sensing dynamic range for Hg^{2+} ions in future studies.

Similarly, Figure 6D illustrates an increase in absorbance at 650 nm with higher Fe^{2+} concentrations. The inset in Figure

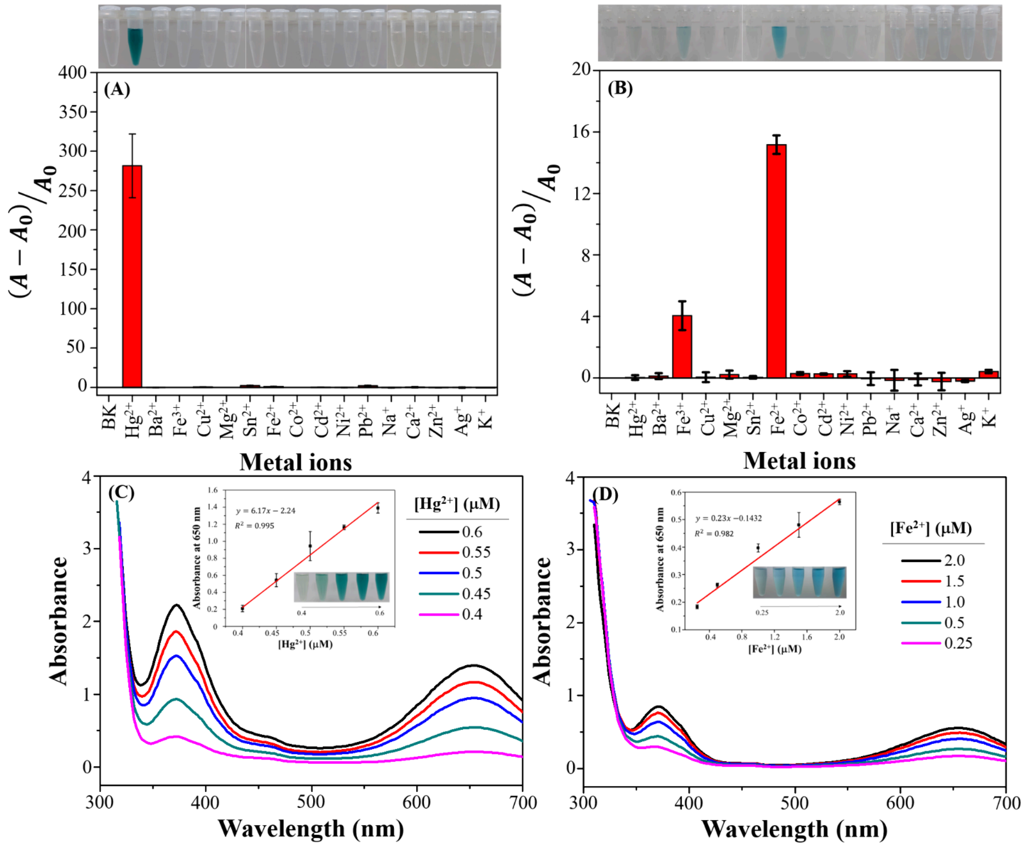

Figure 6. Selectivity and Sensitivity Tests. Selectivity tests with all metal ions at 1.0 μM for (A) TA-AuNPs/H_2O_2/TMB and (B) TA-AuNPs/PDCA/H_2O_2/TMB. UV−vis spectra (inset: linear response plots and images) for (C) TA-AuNPs/H_2O_2/TMB at 0.4−0.6 μM Hg^{2+}, and (D) TA-AuNPs/PDCA/H_2O_2/TMB at 0.25−2.0 μM Fe^{2+} ions (0.1× TA-AuNPs, [PDCA]: 1.0 mM, [H_2O_2]: 50 mM, [TMB]: 1.0 mM).

Table 2. Spiked Recovery (%) and RSD (%) of Detecting Hg^{2+} and Fe^{2+} Ions in Real Samples

Metal ions	Samples	Spiked concentration (μM)	Detected concentration (μM)	Recovery (%)	RSD (%)
Hg^{2+}	lake water	0	Nondetected	-	-
		0.40	0.41	102.5	1.9
		0.50	0.54	108.0	4.6
		0.60	0.61	101.6	3.5
Fe^{2+}	lake water	0	0.48	-	-
		0.40	0.86	95.0	8.9
		0.80	1.20	90.0	7.5
		1.60	2.08	100.0	7.5
	commercial iron supplements	0	0.46	-	-
		0.40	0.91	112.5	6.7
		0.80	1.35	111.3	3.6
		1.60	2.08	101.3	4.8

6D provides a linear range for Fe^{2+} from 0.25 μM to 2.00 μM ($R^2 = 0.982$), with a LOD of 96 nM (5.4 ppb). These findings comply with the discharge standards by Taiwan's Environmental Protection Administration, which require dissolved iron concentrations in industrial effluent not to exceed 10.0 ppm, and WHO, along with Taiwan's drinking water standards, which limit iron concentrations to below 0.30 ppm.[47] Hence, the proposed system can effectively detect Fe^{2+} in industrial wastewater and drinking water. To validate whether the inclusion of TA-AuNPs achieves better detection limits, experiments were also conducted using a PDCA/TMB/H_2O_2 system (data not shown). This system offered a linear range between 0.75−2.00 μM ($R^2 = 0.950$), with a LOD of 0.25 μM, slightly higher than the system incorporating TA-AuNPs. Therefore, this confirms that adding TA-AuNPs enhances the sensitivity and achieves better detection limits for the system.

3.5. Applications. The real-world application of TA-AuNPs/H_2O_2/TMB for ion sensing was assessed using samples from Baisha Lake at the National Changhua University of Education and commercially available iron supplements. After preprocessing, solutions of Hg^{2+} and Fe^{2+} prepared with lake water were analyzed. The detection ranged from 0.40 μM to 0.60 μM for Hg^{2+} ($R^2 = 0.993$) with a LOD of 0.10 μM and from 0.25 μM to 2.00 μM for Fe^{2+} ($R^2 = 0.958$) with a LOD of 0.18 μM. Both systems showed strong linear relationships in real samples, indicating their potential and applicability in environmental water testing. Additionally, Table 2 showed that satisfactory spiked recoveries of 101.6−

Table 3. Comparison of the Analytical Performances for the Present and the Reported Words for the Determination of Hg^{2+} and Fe^{2+} Ions

Target	Probe	Preparation time	Dynamic sensing range	LOD	Real samples	ref
Hg^{2+}	Pt NPs	0.5 h	50−500 nM	16.9 nM	Tap, Ground waters	48
	CS-Se NPs	1 h	0.1−2.5 μM	0.12 μM	-	49
	CuMOF NPs	90 h	0.2−2.0 μM	0.55 μM	-	50
	Fe_3O_4@C@AuNPs	42 h	0.001−25.0 μM	43.5 nM	Tap water	21
	TA-AuNPs	2 min	0.40−0.60 μM	18 nM	Lake water	This study
Fe^{2+}	MB-AuNPs	2.3 h	16.6−1666 nM	11.21 nM	Drinking water	51
	AgNPs	1 h	1−90 μM	0.54 μM	-	52
	mPD-CDs	18 h	1.0−60.0 μM	2.98 μM	-	53
	$MnSiO_3$NPs	21 h	3.0−63.0 μM	0.5 μM	Drinking water	54
	TA-AuNPs/PDCA	2 min	0.25−2.0 μM	96 nM	Lake water, Commercial iron supplement	This study

108.0% for Hg^{2+} with relative standard deviations (RSDs) of 1.9−4.6% and 90.0−100.0% for Fe^{2+} with RSDs of 7.5−8.9%, was noted, further demonstrating the utility of TA-AuNPs in real-sample analysis. Due to random errors, the acceptable spiked recovery is expected to range between 95.0% and 115.0%. Furthermore, this methodology was applied to assess the iron content in commercially available iron supplements. Ground supplements were dissolved, filtered, and tested after dilution. The Fe^{2+} concentration range was established at 0.25−2.00 μM ($R^2 = 0.975$) with a LOD of 0.18 μM, affirming a consistent linear relationship in these supplements. The spiked recoveries were 101.3−112.5% with RSDs of 3.6−6.7%, showcasing the method's effectiveness and practicality in analyzing iron content in commercially available iron supplements (Table 2).

The proposed sensing systems for the determination of Hg^{2+} and Fe^{2+} offer several attractive features compared to the reported works (Table 3): (1) High sensitivity and selectivity: the system demonstrates high sensitivity toward Hg^{2+} and Fe^{2+} ions, attributed to the specific interactions between the TA-AuNPs, PDCA, and the specific ions. This allows for detecting these metals at low concentration levels, making the system suitable for environmental monitoring and safety assessments. (2) Simple and rapid detection: The colorimetric response of the system, due to the catalytic activity of TA-AuNPs, enables visual detection without the need for sophisticated instrumentation, facilitating rapid and straightforward analysis. (3) Environmental compatibility: The proposed system employs water as the solvent, making it an environmentally friendly option for metal ion detection. Additionally, the biocompatibility of TA adds to the eco-friendly nature of the system. (4) Robustness and stability: The TA-AuNPs exhibit robust stability in different environmental conditions, enhancing the reliability and repeatability of the detection results. These features make the proposed sensing systems attractive tools for effectively and efficiently determining Hg^{2+} and Fe^{2+} in real-world applications.

4. CONCLUSIONS

In this study, TA-AuNPs were synthesized using a simple and rapid approach, with the synthesis process requiring only 2 min, and the resulting TA-AuNPs demonstrated excellent stability across a pH range of 5.0−9.0 and at salinity levels below 40 mM. Utilizing TA-AuNPs, we developed two distinct systems for detecting Hg^{2+} and Fe^{2+}, achieving detection limits of 18 nM and 96 nM, respectively. These systems also exhibited impressive spiked recoveries in real-sample analysis, highlighting the potential of TA-AuNPs in detecting environmental water and commercially available iron supplements. Additionally, the study explored the enzymatic kinetics of TA-AuNPs, focusing on their interaction with TMB and H_2O_2, which revealed that both systems preferentially interact with TMB due to lower K_m values, indicating a stronger affinity and suggesting a promising direction for enhancing the catalytic activity of TA-AuNPs. This research not only contributes a novel method to the field of environmental monitoring but also opens new avenues for the selective detection of metal ions in various water sources, underscoring the practicality and potential of TA-AuNPs for broader environmental and health-related applications.

■ ASSOCIATED CONTENT

Supporting Information

The Supporting Information is available free of charge at https://pubs.acs.org/doi/10.1021/acsomega.4c05167.

Figure S1. Stability assessment of TA-AuNPs versus SC-AuNPs. Figure S2. Absorbance at 650 nm for the system in the absence and presence of HQ scavenger (PDF)

■ AUTHOR INFORMATION

Corresponding Author

Yang-Wei Lin − *Department of Chemistry, National Changhua University of Education, Changhua City 50007, Taiwan;* orcid.org/0000-0001-8667-0811; Phone: +886-4-7211190; Email: linywjerry@cc.ncue.edu.tw

Authors

Kun-Yu Sun − *Department of Chemistry, National Changhua University of Education, Changhua City 50007, Taiwan*
Chen-Yu Chueh − *Department of Chemistry, National Changhua University of Education, Changhua City 50007, Taiwan*
Mei-Yao Wu − *School of Post-baccalaureate Chinese Medicine, China Medical University, Taichung 40424, Taiwan*
Tsunghsueh Wu − *Department of Chemistry, University of Wisconsin-Platteville, Platteville, Wisconsin 53818-3099, United States*

Complete contact information is available at: https://pubs.acs.org/10.1021/acsomega.4c05167

Notes

The authors declare no competing financial interest.

■ ACKNOWLEDGMENTS

This study was supported by the Taiwanese National Science and Technology Council (NSTC) under contracts (112-2113-M-018-005) and the Ministry of Education Teaching Practice Research Program under contracts (PMS1120077).

■ REFERENCES

(1) World Health Organization. *Human health effects of benzene, arsenic, cadmium, nickel, lead and mercury: report of an expert consultation*, 2024.

(2) Dong, T.; Li, H. Neurological risks arising from the bioaccumulation of heavy metal contaminants: A focus on mercury. *Environ. Toxicol.* **2024**, *39*, 2692−2705.

(3) De la Ossa, C. A.; Ramírez-Giraldo, A. F.; Arroyo-Alvis, K.; Marrugo-Negrete, J.; Díez, S. Neuropsychological effects and cognitive deficits associated with exposure to mercury and arsenic in children and adolescents of the Mojana region. *Colombia. Environ. Res.* **2023**, *216*, 114467.

(4) Basu, N.; Bastiansz, A.; Dórea, J. G.; Fujimura, M.; Horvat, M.; Shroff, E.; Weihe, P.; Zastenskaya, I. Our evolved understanding of the human health risks of mercury. *Ambio* **2023**, *52* (5), 877−896.

(5) Sawicki, K. T.; De Jesus, A.; Ardehali, H. Iron metabolism in cardiovascular disease: Physiology, mechanisms, and therapeutic Targets. *Circ. Res.* **2023**, *132* (3), 379−396.

(6) Liu, L.; Yan, F.; Yan, H.; Wang, Z. Impact of iron supplementation on gestational diabetes mellitus: A literature review. *Diabetes, Obesity and Metabolism* **2023**, *25* (2), 342−353.

(7) Pavithra, K. G.; SundarRajan, P.; Kumar, P. S.; Rangasamy, G. Mercury sources, contaminations, mercury cycle, detection and treatment techniques: A review. *Chemosphere* **2023**, *312*, 137314.

(8) Montoro-Leal, P.; García-Mesa, J. C.; Morales-Benítez, I.; Vázquez-Palomo, L.; López Guerrero, M. d. M.; Vereda Alonso, E. I. Synthesis of a novel magnetic nanomaterial for the development of a multielemental speciation method of lead, mercury, and vanadium via HPLC-ICP MS. *Microchim. Acta* **2023**, *190* (8), 296.

(9) Oviedo, M. N.; Luján, C. E.; Lemos, A. A.; Botella, M. B.; Llaver, M.; Wuilloud, R. G. An overview of preconcentration techniques combined with inductively coupled plasma mass spectrometry for trace element determination in biological studies. *Anal. Bioanal. Chem.* **2024**, *416*, 2641.

(10) Guo, C.; Lv, L.; Liu, Y.; Ji, M.; Zang, E.; Liu, Q.; Zhang, M.; Li, M. Applied analytical methods for detecting heavy metals in medicinal plants. *Crit. Rev. Anal. Chem.* **2023**, *53* (2), 339−359.

(11) Kanan, S.; Shabnam, A.; Mohamed, A. A.; Abu-Yousef, I. A. Organic luminescent sensor for mercury (II) and iron (III) ions in aqueous solutions. *Chemosensors* **2023**, *11* (5), 308.

(12) Chen, Z.; Zhang, Z.; Qi, J.; You, J.; Ma, J.; Chen, L. Colorimetric detection of heavy metal ions with various chromogenic materials: Strategies and applications. *J. Hazard. Mater.* **2023**, *441*, 129889.

(13) Gul, Z.; Ullah, S.; Khan, S.; Ullah, H.; Khan, M. U.; Ullah, M.; Ali, S.; Altaf, A. A. Recent progress in nanoparticles based sensors for the detection of mercury (II) ions in environmental and biological samples. *Crit. Rev. Anal. Chem.* **2024**, *54* (1), 44−60.

(14) Kusuma, S. A. F.; Harmonis, J. A.; Pratiwi, R.; Hasanah, A. N. Gold nanoparticle-based colorimetric sensors: Properties and application in detection of heavy metals and biological molecules. *Sensors* **2023**, *23* (19), 8172.

(15) Lin, Y.-W.; Huang, C.-C.; Chang, H.-T. Gold nanoparticle probes for the detection of mercury, lead and copper ions. *Analyst* **2011**, *136* (5), 863−871.

(16) Fan, H.; Zhang, R.; Fan, K.; Gao, L.; Yan, X. Exploring the specificity of nanozymes. *ACS Nano* **2024**, *18* (4), 2533−2540.

(17) Bilal, M.; Khaliq, N.; Ashraf, M.; Hussain, N.; Baqar, Z.; Zdarta, J.; Jesionowski, T.; Iqbal, H. M. Enzyme mimic nanomaterials as nanozymes with catalytic attributes. *Colloid Surf. B-Biointerfaces* **2023**, *221*, 112950.

(18) Chen, G.-Y.; Chai, T.-Q.; Wang, J.-L.; Yang, F.-Q. Recent advances in the colorimetric and fluorescence analysis of bioactive small-molecule compounds based on the enzyme-like activity of nanomaterials. *J. Pharm. Biomed. Anal.* **2023**, *236*, 115695.

(19) Issaka, E.; Wariboko, M. A.; Mohammed, A.; Enyan, M.; Aguree, S. Trends in enzyme mimics for enhanced catalytic cascade systems for bio-sensing of environmental pollutants-A review. *Chem. Eng. J. Adv.* **2023**, *15*, 100510.

(20) Liu, D.-M.; Dong, C. Gold nanoparticles as colorimetric probes in food analysis: Progress and challenges. *Food Chem.* **2023**, *429*, 136887.

(21) Motlhaedi, B.; Mokone, J.; Alula, M. T. Enhanced peroxidase-like activity of gold nanoparticles loaded on carbon coated magnetic nanoparticles for colorimetric detection of mercury (II). *Inorg. Chem. Commun.* **2023**, *156*, 111296.

(22) Shamsabadi, A.; Haghighi, T.; Carvalho, S.; Frenette, L. C.; Stevens, M. M. The nanozyme revolution: Enhancing the performance of medical biosensing platforms. *Adv. Mater.* **2024**, *36*, 2300184.

(23) Perwez, M.; Lau, S. Y.; Hussain, D.; Anboo, S.; Arshad, M.; Thakur, P. Nanozymes and nanoflower: Physiochemical properties, mechanism and biomedical applications. *Colloid Surf. B-Biointerfaces* **2023**, *225*, 113241.

(24) Zhang, L.; Bi, X.; Liu, X.; He, Y.; Li, L.; You, T. Advances in the application of metal−organic framework nanozymes in colorimetric sensing of heavy metal ions. *Nanoscale* **2023**, *15* (31), 12853−12867.

(25) Khoshbin, Z.; Moeenfard, M.; Abnous, K.; Taghdisi, S. M. A label-free aptasensor for colorimetric detection of food toxin: Mediation of catalytically active gold nanozymes and smartphone imaging strategy. *Food Chem.* **2024**, *433*, 137355.

(26) Li, Q.; Li, H.; Li, K.; Gu, Y.; Wang, Y.; Yang, D.; Yang, Y.; Gao, L. Specific colorimetric detection of methylmercury based on peroxidase-like activity regulation of carbon dots/Au NPs nanozyme. *J. Hazard. Mater.* **2023**, *441*, 129919.

(27) Ali, Z.; Ullah, R.; Tuzen, M.; Ullah, S.; Rahim, A.; Saleh, T. A. Colorimetric sensing of heavy metals on metal doped metal oxide nanocomposites: A review. *Trends Environ. Anal. Chem.* **2023**, *37*, No. e00187.

(28) Do Dat, T.; Cong, C. Q.; Le Hoai Nhi, T.; Khang, P. T.; Nam, N. T. H.; Thi Tinh, N.; Hue, D. T.; Hieu, N. H. Green synthesis of gold nanoparticles using *Andrographis paniculata* leave extract for lead ion detection, degradation of dyes, and bioactivities. *Biochem. Eng. J.* **2023**, *200*, 109103.

(29) Yuan, X.; Ge, L.; Zhou, H.; Tang, J. Size, composition, and surface capping-dependent catalytic activity of spherical gold nanoparticles. *Spectroc. Acta Pt. A-Mol. Biomol. Spectr.* **2023**, *287*, 122082.

(30) Singh, S.; Rai, N.; Tiwari, H.; Gupta, P.; Verma, A.; Kumar, R.; Kailashiya, V.; Salvi, P.; Gautam, V. Recent advancements in the formulation of nanomaterials-based nanozymes, their catalytic activity, and biomedical applications. *ACS Appl. Bio Mater.* **2023**, *6* (9), 3577−3599.

(31) Geleta, G. S. A colorimetric aptasensor based on two dimensional (2D) nanomaterial and gold nanoparticles for detection of toxic heavy metal ions: A review. *Food Chem. Adv.* **2023**, *2*, 100184.

(32) Miola, M.; Multari, C.; Kostevšek, N.; Gerbaldo, R.; Laviano, F.; Verné, E. Tannic-acid-mediated synthesis and characterization of magnetite−gold nanoplatforms for photothermal therapy. *Nanomedicine* **2023**, *18* (20), 1331−1342.

(33) Shao, Y.-C.; Hsieh, M.-M.; Liu, C.-C.; Wang, W.-Y.; Xue, P.-H.; Hu, C.-C.; Chiu, T.-C. Enhanced catalytic activity of tannic acid functionalized gold nanorods toward the reduction of 4-nitrophenol. *J. Mol. Struct.* **2024**, *1303*, 137645.

(34) Serebrennikova, K. V.; Komova, N. S.; Berlina, A. N.; Zherdev, A. V.; Dzantiev, B. B. Tannic acid-capped gold nanoparticles as a novel nanozyme for colorimetric determination of Pb^{2+} ions. *Chemosensors* **2021**, *9* (12), 332.

(35) Krzyzowska, M.; Tomaszewska, E.; Ranoszek-Soliwoda, K.; Bien, K.; Orlowski, P.; Celichowski, G.; Grobelny, J. Tannic acid

modification of metal nanoparticles: Possibility for new antiviral applications. *Nanostructures for oral medicine* **2017**, 335−363.

(36) Lin, Y.-W.; Liu, C.-W.; Chang, H.-T. DNA functionalized gold nanoparticles for bioanalysis. *Anal. Methods* **2009**, *1* (1), 14−24.

(37) Lin, Y. R.; Hsieh, I. C.; Chang, W. H.; Wu, T.; Sun, K. Y.; Lin, Y. W. Tannic acid as a chemosensor for colorimetric detection of Fe (II) and Au (III) ions in environmental water samples. *J. Chin. Chem. Soc.* **2022**, *69* (3), 549−556.

(38) Luo, Y.; Barwa, T. N.; Dempsey, E.; Karthik, R.; Shim, J.; Sukanya, R.; Breslin, C. B. Electrochemical detection of sulfanilamide using tannic acid exfoliated MoS_2 nanosheets combined with reduced graphene oxide/graphite. *Environ. Res.* **2024**, *248*, 118391.

(39) Zhao, Y.; Xu, L.; Kong, F.; Yu, L. Design and preparation of poly (tannic acid) nanoparticles with intrinsic fluorescence: a sensitive detector of picric acid. *Chem. Eng. J.* **2021**, *416*, 129090.

(40) Henglein, A.; Giersig, M. Optical and chemical observations on gold−mercury nanoparticles in aqueous solution. *J. Phys. Chem. B* **2000**, *104* (21), 5056−5060.

(41) Iwahashi, H.; Kawamori, H.; Fukushima, K. Quinolinic acid, α-picolinic acid, fusaric acid, and 2, 6-pyridinedicarboxylic acid enhance the Fenton reaction in phosphate buffer. *Chem.-Biol. Interact.* **1999**, *118* (3), 201−215.

(42) Zhang, H.; Wu, S.; Song, Z.; Fang, L.; Wang, H.-B. Tannic acid-accelerated fenton chemical reaction amplification for fluorescent biosensing: The proof-of-concept towards ultrasensitive detection of DNA methylation. *Talanta* **2023**, *265*, 124811.

(43) Lin, Y.-W.; Cheng, P.-Y.; Tsai, J.-C.; Li, C.-F.; Chou, C.-H.; You, P.-Y.; Hsu, N.-Y.; Wang, C.-I.; Lai, C.-L. A colorimetric sensing of Hg (II) ions using 3-mercaptopropionic acid modified Au nanoparticles for the undergraduate chemistry laboratory curriculum. *J. Nano Edu.* **2015**, *7* (1), 1−9.

(44) Huang, C. C.; Yang, Z.; Lee, K. H.; Chang, H. T. Synthesis of highly fluorescent gold nanoparticles for sensing mercury (II). *Angew. Chem.-Int. Ed.* **2007**, *119* (36), 6948−6952.

(45) Huang, C.-C.; Chang, H.-T. Selective gold-nanoparticle-based "turn-on" fluorescent sensors for detection of mercury (II) in aqueous solution. *Anal. Chem.* **2006**, *78* (24), 8332−8338.

(46) Li, W.; Wang, F.; Shi, Y.; Yu, L. Polyaniline-supported tungsten-catalyzed oxidative deoximation reaction with high catalyst turnover number. *Chin. Chem. Lett.* **2023**, *34* (1), 107505.

(47) Malhotra, N.; Chen, J.-R.; Sarasamma, S.; Audira, G.; Siregar, P.; Liang, S.-T.; Lai, Y.-H.; Lin, G.-M.; Ger, T.-R.; Hsiao, C.-D. Ecotoxicity assessment of Fe_3O_4 magnetic nanoparticle exposure in adult zebrafish at an environmental pertinent concentration by behavioral and biochemical testing. *Nanomaterials* **2019**, *9* (6), 873.

(48) Kora, A. J.; Rastogi, L. Peroxidase activity of biogenic platinum nanoparticles: A colorimetric probe towards selective detection of mercuric ions in water samples. *Sens. Actuator B-Chem.* **2018**, *254*, 690−700.

(49) Cao, H.; Xiao, J.; Liu, H. Enhanced oxidase-like activity of selenium nanoparticles stabilized by chitosan and application in a facile colorimetric assay for mercury (II). *Biochem. Eng. J.* **2019**, *152*, 107384.

(50) Kirandeep; Kaur, J.; Sharma, I.; Zangrando, E.; Pal, K.; Mehta, S. K.; Kataria, R. Fabrication of novel copper MOF nanoparticles for nanozymatic detection of mercury ions. *J. Mater. Res. Technol-JMRT* **2023**, *22*, 278−291.

(51) Salimi, F.; Kiani, M.; Karami, C.; Taher, M. A. Colorimetric sensor of detection of Cr (III) and Fe (II) ions in aqueous solutions using gold nanoparticles modified with methylene blue. *Optik* **2018**, *158*, 813−825.

(52) Basiri, S.; Mehdinia, A.; Jabbari, A. A sensitive triple colorimetric sensor based on plasmonic response quenching of green synthesized silver nanoparticles for determination of Fe^{2+}, hydrogen peroxide, and glucose. *Colloid Surf. A-Physicochem. Eng. Asp.* **2018**, *545*, 138−146.

(53) Sun, X.; Zhang, J.; Wang, X.; Zhao, J.; Pan, W.; Yu, G.; Qu, Y.; Wang, J. Colorimetric and fluorimetric dual mode detection of Fe^{2+} in aqueous solution based on a carbon dots/phenanthroline system. *Arab. J. Chem.* **2020**, *13* (4), 5075−5083.

(54) Wang, T.; Jiang, H.; Bai, Q.; Xiao, H.; Liu, M.; Sui, N. Oxidative properties and utility of fabricated $MnSiO_3$ nanoparticles for colorimetric detection of iron (II) in water samples. *Micro Nano Lett.* **2020**, *15* (12), 808−811.